Magneto-optical effects of an artificially-layered ferromagnetic topological insulator with T_C of 160 K

Xingyue Han,[1] Hee Taek Yi,[2] Seongshik Oh,[2] and Liang Wu[1,*]

[1] *Department of Physics and Astronomy, University of Pennsylvania, Philadelphia, Pennsylvania 19104, USA*
[2] *Department of Physics and Astronomy, Rutgers, The State University of New Jersey, Piscataway, New Jersey 08854, USA*

Abstract: Magnetic topological insulator is a fertile platform to study the interplay between magnetism and topology. The unique electronic band structure can induce exotic transport and optical properties. However, a comprehensive optical study in both near-infrared frequency and terahertz frequency has been lacking. Here, we report magneto-optical effects from a heterostructure of Cr-incorporated topological insulator, CBST. We use 800 nm magneto-optical Kerr effect to reveal a ferromagnetic order in the CBST film with a high transition temperature at 160 K. We also use time-domain terahertz polarimetry to reveal a terahertz Faraday rotation of 1.5 mrad and Kerr rotation of 5.1 mrad at 2 K. The calculated terahertz Hall conductance is 0.42 e^2/h. Our work shows the optical responses of an artificially layered magnetic topological insulator, paving the way towards high-temperature quantum anomalous Hall effect via heterostructure engineering.

key words: magnetic topological insulators, magneto-optical Kerr effect, terahertz Faraday rotation, terahertz Kerr rotation

Topological insulators (TIs), characterised by the insulating bulk states and conducting topological surface states, were originally proposed in time-reversal-invariant systems [1–4]. The gapless topological surface states are located in the bulk gap crossing at the Dirac point. Incorporating ferromagnetism into TIs breaks time-reversal symmetry and opens an exchange gap at the Dirac point [4–6]. The interplay between magnetism and topology has brought a plethora of exotic phenomena [4, 5, 7–10], including the quantum anomalous Hall effect (QAHE) [6], and the axion insulator states [11]. When the Fermi energy lies in the exchange gap, the QAHE emerges due to dissipationless chiral edge modes. In an ideal quantum anomalous Hall state, the anomalous Hall resistance is quantized at h/e^2, while the longitudinal resistivity vanishes. In order to realize a ferromagnetic TI system, the first attempt was doping nonmagnetic TIs with magnetic impurities, such as Cr- and V- doped $(Bi,Sb)_2Te_3$ [6, 12, 13]. However, the inhomogeneity of the magnetic dopants suppresses the effective energy gap. It results in a low observation temperature of QAHE, usually below 100 mK. Following the magnetic impurity doping method, the magnetic modulation doping technique increased the surface mass gap and improved the homogeneity. The QAHE observation temperature was raised to 2 K [14–18]. Recently, intrinsic magnetic TIs with chemical formulas such as $MnBi_2Se4$ [19–21] have received more attention with the report of 97% quantization persist up to 6.5 K in a 5 septuple-layer (SL) flake[20].

The tunability of the magnetic and topological properties of magnetic TIs have been investigated in various ways, such as Sb doping [22, 23], hydrostatic pressure [24, 25], and surface engineering [26]. Another important method is using nonmagnetic spacer layer [27]. For example, in the intrinsic $MnBi_2Te_4$ family, due to the van der Waals nature, the magnitude of interlayer antiferromagnetic strength can be suppressed by inserting Bi_2Te_3 quintuple layers (QL) between $MnBi_2Te_4$ SLs, with the chemical formula $MnBi_{2n}Te_{3n+1}$. The electric band structure spontaneously changes with different magnetic orders. For example, $MnBi_2Te_4$ (n=1) [20] and $MnBi_4Te_7$ (n=2) [23] are reported to be antiferromagnetic TIs, $MnBi_8Te_{13}$ (n=4) is predicted to be ferromagnetic TI [28, 29]. With the boost of research interest in the $MnBi_{2n}Te_{3n+1}$ family, replacing Mn with other magnetic elements has been investigated as well. Density functional theory (DFT) calculations revealed that certain elements can form stable XBi_2Te_4 SL structures, including X = Ti, V, Ni, Eu, etc [21]. But X = Cr, Fe, and Co show instability to form SL structures [21].

Heterostructure engineering is a powerful tool to tune the magnetic and topological properties of Cr-incorporated TIs [27, 30–32]. In our work, we report a heterostructure of Cr-incorporated topological insulator, dubbed as CBST. The layer-by-layer epitaxial deposition of each Sb_2Te_3, Bi_2Te_3 and CrTe was carried out based on the $Cr(Bi_{1/3}Sb_{2/3})_6Te_{10}$ structure (Fig.1**a**). We performed magneto-optical measurements in both near-infrared (NIR) and terahertz (THz) frequencies. Ferromagnetic order is observed using magneto-optical Kerr effect (MOKE). The magnetic transition temperature at 160 K is higher than any other Cr-incorporated magnetic TIs. We also performed THz measurements in CBST which exhibits a Faraday rotation of 1.5 mrad and Kerr rotation of 5.1 mrad under 6 T at 2 K.

In the CBST film, the $Cr(Bi_{1/3}Sb_{2/3})_6Te_{10}$ structure repeats twice, terminating at $(Bi_{1/2}Sb_{1/2})_2Te_3$ (BST) layer (Fig.1**a**). The 6.5 nm-thick film is grown on a 1 cm × 1 cm Al_2O_3 (0001) substrate using a custom-built molecular beam epitaxy (MBE) system (SVTA) under a base pressure of 5×10^{-10} Torr. High-purity (99.999%) Bi,Sb, Te, and Cr were thermally evaporated

* liangwu@sas.upenn.edu

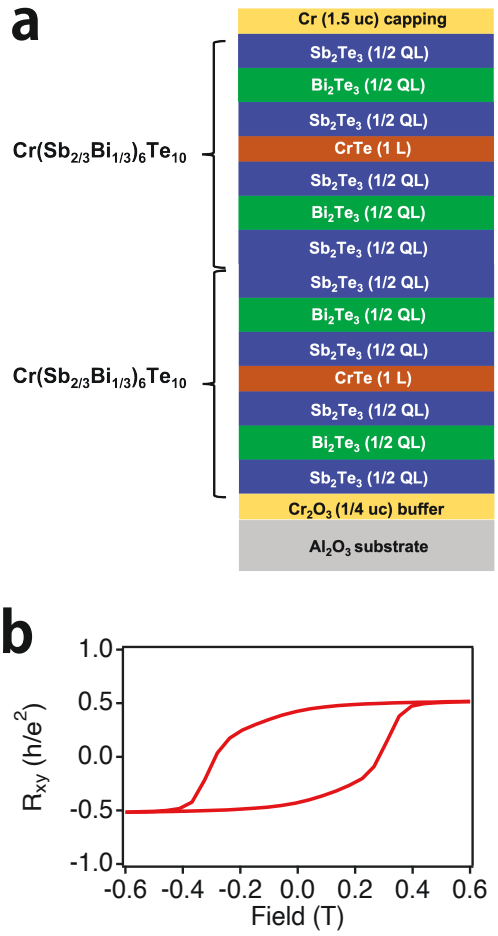

FIG. 1: **Structure and transport of CBST. a.** Layered structure of CBST. The 17-tuple layer structure is repeated twice. The film terminates at BST layer. **b.** Magnetic field dependence of Hall resistance of CBST measured at 2 K.

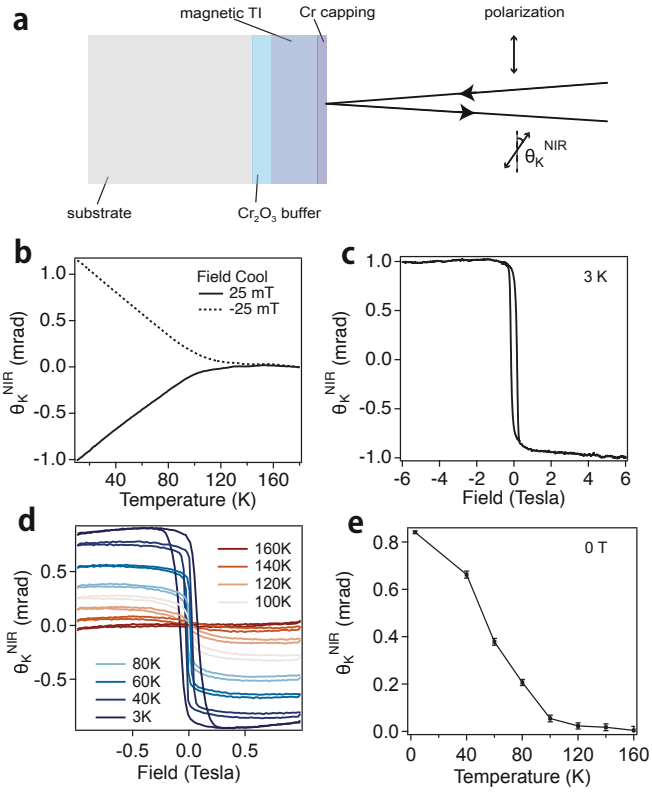

FIG. 2: **MOKE results of CBST at 800 nm. a.** Schematic of MOKE measurement from CBST. **b.** Temperature dependent MOKE under field-cool. ±25 mT magnetic field is applied perpendicular to the sample surface. **c.** MOKE Hysteresis loop measured at 3 K. **d.** MOKE hysteresis loops measured from 3 K to 160 K. **e.** Temperature dependence of the field-symetrized θ_K at 0 T.

using effusion cells, and all the source fluxes were calibrated in-situ by quartz crystal micro-balance and ex-situ by Rutherford backscattering spectroscopy. We employ thin epitaxial Cr_2O_3 as a buffer layer to assist the topological layers in adhering to the Al_2O_3 substrate, and naturally oxidized amorphous CrO_x as a capping layer to suppress degradation and boost ferromagnetic order [18, 27]. High-angle annular dark-field scanning transmission electron microscope (HAADF-STEM) image has revealed that Cr is incorporated into the neighboring Sb_2Te_3 layer instead of forming a van der Waals gap between Sb_2Te_3 layers [27]. The transport data at 2 K (Fig.1**b**) with single coercive field inicates that surface states only form at top and bottom surfaces, suggesting that the entire system is behaving as a single magnetic TI layer.

We firstly utilize MOKE to probe the time-reversal symmetry breaking in CBST. A mode-locked Ti:sapphire laser with 800 nm centre wavelength, 80 MHz repetition rate and 50 fs pulse duration is used to measure the Kerr rotation θ_K^{NIR} from the CBST sample [33]. θ_K^{NIR} is the polarization plane change in the reflection beam proportional to the net magnetization along the laser propagation direction [34] (Fig.2**a**). We carried out temperature dependent MOKE measurements under an out-of-plane magnetic field at ± 25 mT. As shown in Fig.2**b**, cooling from 180 K to 10 K, θ_K^{NIR} emerges around 160 K and shows opposite signs under opposite magnetic fields. Fig.2**c** and **d** show the magnetic field dependent MOKE at 3 K and higher temperatures. θ_K^{NIR} at 3 K shows a hysteresis loop with the coercive field H_C at 70 mT and saturates at 1 mrad. Above the saturation field, there is no signs of spin-flip/flop transitions up to ± 6 T, consistent with the behavior from a ferromagnetic order. The coercive field and MOKE signal monotonically decrease with increasing temperature, and disappears at 160 K (Fig.2**d**). Fig.2**e** shows zero-field MOKE

$$\theta_K^{NIR}(0T) = \frac{\theta_K^{NIR}(+0T) - \theta_K^{NIR}(-0T)}{2} \qquad (1)$$

under different temperatures. The high transition temperature indicates an enhanced ferromagnetic order in the CBST film, compared to other Cr-incorporated magnetic TIs (TABLE.I), achieved by the high Cr concentration from the layer-by-layer growth method and an active capping layer CrO_x [18, 27]. Note that our table does not include other dopants to compare different growth method and heterostructures [12, 35, 36] or heavily ferromagnetic doped bulk samples due to possible clustering [4, 37] .

Type	Sample	T_N/T_C
Intrinsic	$MnBi_2Te_4$[38–41]	15-25 K
	$MnBi_6Te_{10}$*[42]	13 K
	$MnBi_8Te_{13}$*[28]	10 K
Uniform doping	$Cr_{0.15}(Bi_{0.1}Sb_{0.9})_{1.85}Te_3$ [6]	15 K
	$Cr_{0.22}(Bi_{0.2}Sb_{0.8})_{1.78}Te_3$ [13]	45 K
	$Cr_{0.29}Sb_{1.71}Te_3$ [12]	59 K
Modulation doping	$Cr_{0.57}(Bi_{0.26}Sb_{0.74})_{1.43}Te_3$ [43]	70 K
	$Cr_{0.95}(Bi_{0.32}Sb_{0.68})_{1.05}Te_3$ [14]	80 K
	layered heterostructure (this work)	160 K

TABLE I: Magnetic transition temperatures of $MnBi_{2n}Te_{3n+1}$ family and Cr-incorporated magnetic TIs.

Then we study the low-energy response of CBST film by transmission time-domain terahertz (THz) polarimetry from 0.2 THz (0.8 meV) to 1.2 THz (5.0 meV) [44]. A pair of photoconductive antennas are used to generate and probe THz radiations. A delay stage introducing time delay between THz emission and the detection path enables the time-domain measurement. A THz polarizer mounted on a rotation stage is used to analyze THz polarization transmitted through the CBST film. In magnetic TIs, the exchange energy gap opening at the TI surface is usually tens of meV [45, 46]. Thus interband transition is prohibited under THz excitation. We then measure the THz Faraday $\theta_{\rm F}^{\rm THz}$ and Kerr rotation $\theta_{\rm K}^{\rm THz}$ from CBST film. By definition, Faraday rotation refers to the polarization change of the transmitted light, while Kerr rotation is about the reflected light. In the time-domain spectroscopy, the transmitted light is composed of the main pulse and a series of echos which are separated in time (Fig.3**b**). The main pulse is the directly transmitted THz wave (Fig.3**a**). The first echo is firstly reflected at the substrate/TI interface, then reflected back at the substrate surface, finally transmitted through the film (Fig.3**a**). Higher orders of echos appear later in time, and are not being considered here. Therefore, the polarization change of the main pulse is the Faraday rotation $\theta_{\rm F}^{\rm THz}$ (Fig.3**a,b**). The polarization change of the first echo is the sum of Faraday rotation and Kerr rotation $\Theta^{THz} = \theta_{\rm F}^{\rm THz} + \theta_{\rm K}^{\rm THz}$ (Fig.3**a,b**). Here we use the superscript "THz" to distinguish the THz rotations with the NIR MOKE results in Fig.2. By fixing the incident polarization (x direction), the THz rotation angles can be calculated from the ratio of the perpendicular component (E_y) and the parallel component (E_x).

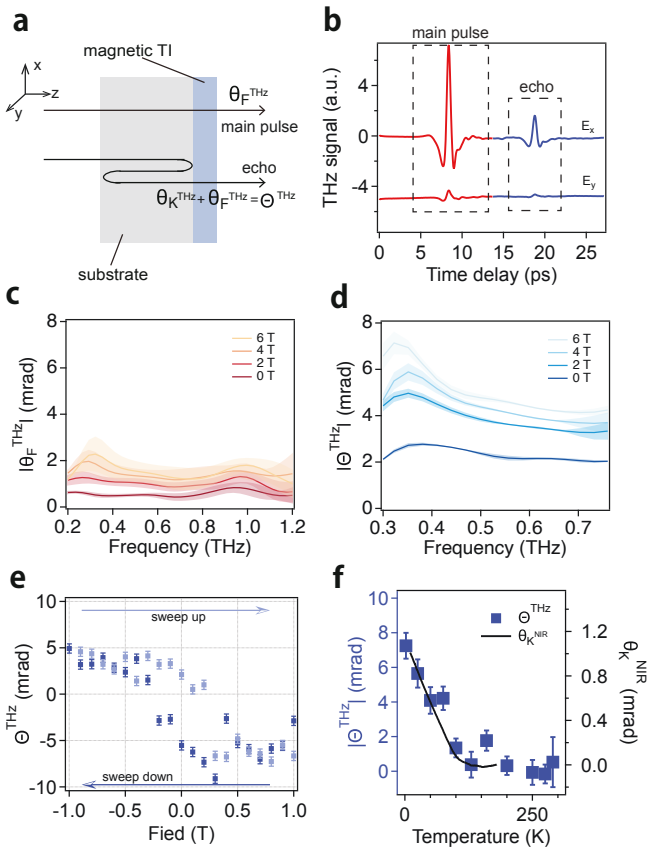

FIG. 3: **THz result of CBST. a.** Schematics of the polarization state of the transmitted THz waves after CBST. The incident THz polarization is parallel to x-axis. **b.** Terahertz signals in time domain for the CBST. The transmitted light is composed of the main pulse and the first echo. They are separated in time domain due to different light path. E_x and E_y are the transmitted signals parallel and perpendicular, respectively, to the incident polarization at 0 T. **c.** Spectra of THz Faraday rotation at 2 K. **d.** Spectra of Θ^{THz}, the sum of THz Faraday rotation $\theta_{\rm F}^{\rm THz}$ and THz Kerr rotation, at 2 K. The shaded area in **c** and **d** are error bars. **e.** Field dependence of Θ^{THz} at 2 K. Each data point is calculated from the average value in the range 0.2 THz to 1.4 THz. **f.** Temperature dependence of Θ^{THz} (blue squares) and θ_K^{NIR} (black curve).

To measure the field-dependence of $\theta_{\rm F}^{\rm THz}$ and Θ^{THz}, the magnetic field is swept to 6 T to magnetize the film before measurements. A sequence of 6 T $\rightarrow$ 4 T $\rightarrow$ 2 T $\rightarrow$ 0 T $\rightarrow$ -6 T $\rightarrow$ -4 T $\rightarrow$ -2 T $\rightarrow$ 0 T is followed to apply the field. Fig.3**c** displays the field-symmetrized THz Faraday and Kerr rotation spectra

$$\theta_{\rm F}^{\rm THz}(B) = \frac{\theta_{\rm F}^{\rm THz}(+B) - \theta_{\rm F}^{\rm THz}(-B)}{2} \qquad (2)$$

at 2 K. A modest frequency dependence agrees with previous THz measurements in magnetic TIs [31, 43]. Under 0 T, $\theta_{\rm F}^{\rm THz}$ shows an average value of 0.57 mrad. It

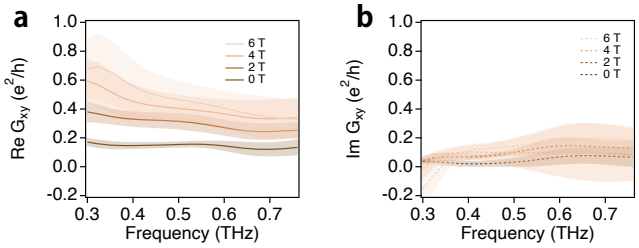

FIG. 4: **THz anomalous Hall conductance of CBST.** G_{xy} is the complex anomalous Hall conductivity. **a.** and **b.** shows the real and imaginary part of the 2K G_{xy}, respectively. Shaded area is the error bar.

increases monotonically with magnetic field and reaches 1.5 mrad under 6 T. Field-symmetrized spectra of Θ^{THz} in the range 0.3 THz (1.2 meV) to 0.76 THz (3.1 meV) are displayed in Fig.3**d**. The more substantial frequency dependence of Θ^{THz} at high fields comes from the temporal overlap between the main pulse and the echo [43]. The average value of Θ^{THz} is 2.3 mrad under 0 T and 5.1 mrad under 6 T. The field and temperature dependence of Θ^{THz} are displayed in Fig.3**e** and **f**. A hysteresis loop is observed in Θ^{THz}, and its temperature dependence well agrees with θ_K^{NIR}. These observations corroborates the magnetic origin of the THz rotations in CBST.

THz Faraday rotation is related to THz Hall conductance G_{xy} via

$$G_{xy} = \theta_{\mathrm{F}}^{\mathrm{THz}}(G_{xx} + \frac{n_s + 1}{Z_0}) \tag{3}$$

Here G_{xx} is the longitudinal conductance, n_s is the refractive index of the substrate (3.1 for sapphire), and Z_0 ($\approx$376.7 Ω) is the vacuum impedance. We obtain a small G_{xx} in the probing frequency range from the nearly unity THz transmission T_{xx}, according to

$$G_{xx} = \frac{n_s + 1}{Z_0}[\frac{e^{i\omega(n_s-1)\Delta L/c}}{T_{xx}} - 1] \tag{4}$$

Here c is the speed of light, and ΔL is the thickness mismatch between the CBST sample and reference substrate. As shown in Fig.4**a.**, the Hall conductance is almost constant at 0.14 e^2/h under 0 T. Under higher magnetic fields, G_{xy} decreases at higher frequencies. Under 6 T, G_{xy} reaches a maximum value of 0.69 e^2/h at 0.32 THz, and converges to 0.33 e^2/h at 0.7 THz. The average value of the 6 T spectrum is 0.42 e^2/h. The frequency dependence at high field might come from cyclotron resonances[47, 48]. A small but nonzero value in the imaginary part of the complex G_{xy} (Fig.4**b.**) also indicates the emergence of dissipation.

In the ideal QAHE state, G_{xx} vanishes to zero, while G_{xy} is quantized in unit of e^2/h. The calculated THz Faraday and Kerr rotations are $tan^{-1}(\frac{2\alpha}{n_s+1})$ = 3.67 mrad and $tan^{-1}(\frac{4n_s\alpha}{n_s^2-1})$ = 10.5 mrad, respectively [31, 43, 47]. To account for the deviation between experimental results and theoretical calculations, different reasons were proposed such as trivial bands involvement [35, 49] and emergence of superparamagnetic order [49, 50]. Further investigation in CBST about the Fermi level and possible superparamagnetic order are needed towards the realization of QAHE . Looking forward, we hope this work generate interests in realizing high-temperature QAHE at terahertz frequency.

Acknowledgments This project at Penn and Rutgers is mainly sponsored by the Army Research Office and was accomplished under Grant Number W911NF-20-2-0166. X.H. is also partially supported by the Gordon and Betty Moore Foundation's EPiQS Initiative, Grant GBMF9212 to L.W. and the NSF EPM program under grant no. DMR-2213891 for manuscript writing. The work at Rutgers by H. Yi and S. O. was also supported by NSF DMR2004125, and the center for Quantum Materials Synthesis (cQMS), funded by the Gordon and Betty Moore Foundation's EPiQS initiative through grant GBMF10104. It is supported in part by grant NSF PHY-1748958 to the Kavli Institute for Theoretical Physics (KITP).

REFERENCES

[1] Moore, J. E. The birth of topological insulators. *Nature* **2010**, *464*, 194–198.
[2] Hasan, M. Z.; Kane, C. L. Colloquium: topological insulators. *Reviews of modern physics* **2010**, *82*, 3045.
[3] Qi, X.-L.; Zhang, S.-C. Topological insulators and superconductors. *Rev. Mod. Phys.* **2011**, *83*, 1057–1110.
[4] Tokura, Y.; Yasuda, K.; Tsukazaki, A. Magnetic topological insulators. *Nature Reviews Physics* **2019**, *1*, 126–143.
[5] Yu, R.; Zhang, W.; Zhang, H.-J.; Zhang, S.-C.; Dai, X.; Fang, Z. Quantized anomalous Hall effect in magnetic topological insulators. *science* **2010**, *329*, 61–64.
[6] Chang, C.-Z.; Zhang, J.; Feng, X.; Shen, J.; Zhang, Z.; Guo, M.; Li, K.; Ou, Y.; Wei, P.; Wang, L.-L., et al. Experimental observation of the quantum anomalous Hall effect in a magnetic topological insulator. *Science* **2013**, *340*, 167–170.
[7] Onoda, M.; Nagaosa, N. Quantized anomalous Hall effect in two-dimensional ferromagnets: quantum Hall effect in metals. *Physical review letters* **2003**, *90*, 206601.
[8] Wan, X.; Turner, A. M.; Vishwanath, A.; Savrasov, S. Y. Topological semimetal and Fermi-arc surface states in the electronic structure of pyrochlore iridates. *Physical Review B* **2011**, *83*, 205101.
[9] Nakatsuji, S.; Kiyohara, N.; Higo, T. Large anomalous Hall effect in a non-collinear antiferromagnet at room temperature. *Nature* **2015**, *527*, 212–215.
[10] Armitage, N.; Mele, E.; Vishwanath, A. Weyl and Dirac semimetals in three-dimensional solids. *Reviews of Modern Physics* **2018**, *90*, 015001.
[11] Liu, C.; Wang, Y.; Li, H.; Wu, Y.; Li, Y.; Li, J.; He, K.; Xu, Y.; Zhang, J.; Wang, Y. Robust axion insulator and Chern insulator phases in a two-dimensional antiferro-

magnetic topological insulator. *Nature materials* **2020**, *19*, 522–527.

[12] Chang, C.-Z.; Zhao, W.; Kim, D. Y.; Zhang, H.; Assaf, B. A.; Heiman, D.; Zhang, S.-C.; Liu, C.; Chan, M. H.; Moodera, J. S. High-precision realization of robust quantum anomalous Hall state in a hard ferromagnetic topological insulator. *Nature materials* **2015**, *14*, 473–477.

[13] Checkelsky, J.; Yoshimi, R.; Tsukazaki, A.; Takahashi, K.; Kozuka, Y.; Falson, J.; Kawasaki, M.; Tokura, Y. Trajectory of the anomalous Hall effect towards the quantized state in a ferromagnetic topological insulator. *Nature Physics* **2014**, *10*, 731–736.

[14] Mogi, M.; Yoshimi, R.; Tsukazaki, A.; Yasuda, K.; Kozuka, Y.; Takahashi, K.; Kawasaki, M.; Tokura, Y. Magnetic modulation doping in topological insulators toward higher-temperature quantum anomalous Hall effect. *Applied Physics Letters* **2015**, *107*, 182401.

[15] Mogi, M.; Kawamura, M.; Yoshimi, R.; Tsukazaki, A.; Kozuka, Y.; Shirakawa, N.; Takahashi, K.; Kawasaki, M.; Tokura, Y. A magnetic heterostructure of topological insulators as a candidate for an axion insulator. *Nature materials* **2017**, *16*, 516–521.

[16] Mogi, M.; Kawamura, M.; Tsukazaki, A.; Yoshimi, R.; Takahashi, K. S.; Kawasaki, M.; Tokura, Y. Tailoring tricolor structure of magnetic topological insulator for robust axion insulator. *Science advances* **2017**, *3*, eaao1669.

[17] Ou, Y.; Liu, C.; Jiang, G.; Feng, Y.; Zhao, D.; Wu, W.; Wang, X.-X.; Li, W.; Song, C.; Wang, L.-L., et al. Enhancing the quantum anomalous Hall effect by magnetic codoping in a topological insulator. *Advanced materials* **2018**, *30*, 1703062.

[18] Yi, H. T.; Jain, D.; Yao, X.; Oh, S. Enhanced Quantum Anomalous Hall Effect with an Active Capping Layer. *Nano Letters* **2023**, *23*, 5673–5679.

[19] Otrokov, M. M.; Klimovskikh, I. I.; Bentmann, H.; Estyunin, D.; Zeugner, A.; Aliev, Z. S.; Gaß, S.; Wolter, A.; Koroleva, A.; Shikin, A. M., et al. Prediction and observation of an antiferromagnetic topological insulator. *Nature* **2019**, *576*, 416–422.

[20] Deng, Y.; Yu, Y.; Shi, M. Z.; Guo, Z.; Xu, Z.; Wang, J.; Chen, X. H.; Zhang, Y. Quantum anomalous Hall effect in intrinsic magnetic topological insulator MnBi2Te4. *Science* **2020**, *367*, 895–900.

[21] Li, J.; Li, Y.; Du, S.; Wang, Z.; Gu, B.-L.; Zhang, S.-C.; He, K.; Duan, W.; Xu, Y. Intrinsic magnetic topological insulators in van der Waals layered MnBi2Te4-family materials. *Science Advances* **2019**, *5*, eaaw5685.

[22] Guan, Y. D.; Yan, C. H.; Lee, S. H.; Gui, X.; Ning, W.; Ning, J. L.; Zhu, Y. L.; Kothakonda, M.; Xu, C. Q.; Ke, X. L.; Sun, J. W.; Xie, W. W.; Yang, S. L.; Mao, Z. Q. Ferromagnetic $MnBi_4Te_7$ obtained with low-concentration Sb doping: A promising platform for exploring topological quantum states. *Phys. Rev. Mater.* **2022**, *6*, 054203.

[23] Hu, C.; Lien, S.-W.; Feng, E.; Mackey, S.; Tien, H.-J.; Mazin, I. I.; Cao, H.; Chang, T.-R.; Ni, N. Tuning magnetism and band topology through antisite defects in Sb-doped MnBi 4 Te 7. *Physical Review B* **2021**, *104*, 054422.

[24] Eckberg, C.; Qiu, G.; Qu, T.; Kwon, S.; Liu, Y.; Tai, L.; Graf, D.; Chong, S. K.; Zhang, P.; Wong, K. L.; Lake, R. K.; Neupane, M. R.; Wang, K. L. Structural tuning magnetism and topology in a magnetic topological insulator. 2023; 2110.00540; arXiv: cond-mat.mes-hall; https://arxiv.org/abs/2301.03078, (accessed 2023-12-25).

[25] Chen, K. Y.; Wang, B. S.; Yan, J.-Q.; Parker, D. S.; Zhou, J.-S.; Uwatoko, Y.; Cheng, J.-G. Suppression of the antiferromagnetic metallic state in the pressurized $MnBi_2Te_4$ single crystal. *Phys. Rev. Mater.* **2019**, *3*, 094201.

[26] Mazza, A. R.; Lapano, J.; MeyerIII, H. M.; Nelson, C. T.; Smith, T.; Pai, Y.-Y.; Noordhoek, K.; Lawrie, B. J.; Charlton, T. R.; Moore, R. G., et al. Surface-Driven Evolution of the Anomalous Hall Effect in Magnetic Topological Insulator MnBi2Te4 Thin Films. *Advanced Functional Materials* **2022**, *32*, 2202234.

[27] Yao, X.; Yi, H. T.; Jain, D.; Han, M.-G.; Oh, S. Spacer-layer-tunable magnetism and high-field topological Hall effect in topological insulator heterostructures. *Nano Letters* **2021**, *21*, 5914–5919.

[28] Hu, C.; Ding, L.; Gordon, K. N.; Ghosh, B.; Tien, H.-J.; Li, H.; Linn, A. G.; Lien, S.-W.; Huang, C.-Y.; Mackey, S., et al. Realization of an intrinsic ferromagnetic topological state in MnBi8Te13. *Science advances* **2020**, *6*, eaba4275.

[29] Zhong, H.; Bao, C.; Wang, H.; Li, J.; Yin, Z.; Xu, Y.; Duan, W.; Xia, T.-L.; Zhou, S. Light-tunable surface state and hybridization gap in magnetic topological insulator MnBi8Te13. *Nano Letters* **2021**, *21*, 6080–6086.

[30] Jiang, J.; Xiao, D.; Wang, F.; Shin, J.-H.; Andreoli, D.; Zhang, J.; Xiao, R.; Zhao, Y.-F.; Kayyalha, M.; Zhang, L., et al. Concurrence of quantum anomalous Hall and topological Hall effects in magnetic topological insulator sandwich heterostructures. *Nature Materials* **2020**, *19*, 732–737.

[31] Mogi, M.; Okamura, Y.; Kawamura, M.; Yoshimi, R.; Yasuda, K.; Tsukazaki, A.; Takahashi, K.; Morimoto, T.; Nagaosa, N.; Kawasaki, M., et al. Experimental signature of the parity anomaly in a semi-magnetic topological insulator. *Nature Physics* **2022**, *18*, 390–394.

[32] Yasuda, K.; Wakatsuki, R.; Morimoto, T.; Yoshimi, R.; Tsukazaki, A.; Takahashi, K.; Ezawa, M.; Kawasaki, M.; Nagaosa, N.; Tokura, Y. Geometric Hall effects in topological insulator heterostructures. *Nature Physics* **2016**, *12*, 555–559.

[33] Xu, Y.; Ni, Z.; Liu, Y.; Ortiz, B. R.; Deng, Q.; Wilson, S. D.; Yan, B.; Balents, L.; Wu, L. Three-state nematicity and magneto-optical Kerr effect in the charge density waves in kagome superconductors. *Nature physics* **2022**, *18*, 1470–1475.

[34] McCord, J. Progress in magnetic domain observation by advanced magneto-optical microscopy. *Journal of Physics D: Applied Physics* **2015**, *48*, 333001.

[35] Li, W.; Claassen, M.; Chang, C.-Z.; Moritz, B.; Jia, T.; Zhang, C.; Rebec, S.; Lee, J.; Hashimoto, M.; Lu, D.-H., et al. Origin of the low critical observing temperature of the quantum anomalous Hall effect in V-doped (Bi, Sb) 2Te3 film. *Scientific reports* **2016**, *6*, 32732.

[36] Liu, C.; Zang, Y.; Ruan, W.; Gong, Y.; He, K.; Ma, X.; Xue, Q.-K.; Wang, Y. Dimensional Crossover-Induced Topological Hall Effect in a Magnetic Topological Insulator. *Phys. Rev. Lett.* **2017**, *119*, 176809.

[37] Wimmer, S. et al. Mn-Rich MnSb2Te4: A Topological Insulator with Magnetic Gap Closing at High Curie Temperatures of 45–50 K. *Advanced Materials* **2021**, *33*,

2102935.

[38] Gong, Y.; Guo, J.; Li, J.; Zhu, K.; Liao, M.; Liu, X.; Zhang, Q.; Gu, L.; Tang, L.; Feng, X., et al. Experimental realization of an intrinsic magnetic topological insulator. *Chinese Physics Letters* **2019**, *36*, 076801.

[39] Zhao, Y.-F.; Zhou, L.-J.; Wang, F.; Wang, G.; Song, T.; Ovchinnikov, D.; Yi, H.; Mei, R.; Wang, K.; Chan, M. H. W.; Liu, C.-X.; Xu, X.; Chang, C.-Z. Even–Odd Layer-Dependent Anomalous Hall Effect in Topological Magnet MnBi2Te4 Thin Films. *Nano Letters* **2021**, *21*, 7691–7698, PMID: 34468149.

[40] Liu, S.; Yu, J.; Zhang, E.; Li, Z.; Sun, Q.; Zhang, Y.; Li, L.; Zhao, M.; Leng, P.; Cao, X.; Zou, J.; Kou, X.; Zang, J.; Xiu, F. Gate-tunable Intrinsic Anomalous Hall Effect in Epitaxial MnBi2Te4 Films. 2021; 2110.00540; arXiv: cond-mat.mtrl-sci; http://arxiv.org/abs/2110.00540, (accessed 2023-12-25).

[41] Liu, N.; Schreyeck, S.; Fijalkowski, K.; Kamp, M.; Brunner, K.; Gould, C.; Molenkamp, L. Antiferromagnetic order in MnBi2Te4 films grown on Si(1 1 1) by molecular beam epitaxy. *Journal of Crystal Growth* **2022**, *591*, 126677.

[42] Yan, C.; Zhu, Y.; Miao, L.; Fernandez-Mulligan, S.; Green, E.; Mei, R.; Tan, H.; Yan, B.; Liu, C.-X.; Alem, N.; Mao, Z.; Yang, S. Delicate Ferromagnetism in MnBi6Te10. *Nano Letters* **2022**, *22*, 9815–9822, PMID: 36315185.

[43] Okada, K. N.; Takahashi, Y.; Mogi, M.; Yoshimi, R.; Tsukazaki, A.; Takahashi, K. S.; Ogawa, N.; Kawasaki, M.; Tokura, Y. Terahertz spectroscopy on Faraday and Kerr rotations in a quantum anomalous Hall state. *Nature communications* **2016**, *7*, 1–6.

[44] Han, X.; Markou, A.; Stensberg, J.; Sun, Y.; Felser, C.; Wu, L. Giant intrinsic anomalous terahertz Faraday rotation in the magnetic Weyl semimetal Co_2MnGa at room temperature. *Phys. Rev. B* **2022**, *105*, 174406.

[45] Lee, I.; Kim, C. K.; Lee, J.; Billinge, S. J.; Zhong, R.; Schneeloch, J. A.; Liu, T.; Valla, T.; Tranquada, J. M.; Gu, G., et al. Imaging Dirac-mass disorder from magnetic dopant atoms in the ferromagnetic topological insulator Crx (Bi0. 1Sb0. 9) 2-xTe3. *Proceedings of the National Academy of Sciences* **2015**, *112*, 1316–1321.

[46] Chen, Y.; Chu, J.-H.; Analytis, J.; Liu, Z.; Igarashi, K.; Kuo, H.-H.; Qi, X.; Mo, S.-K.; Moore, R.; Lu, D., et al. Massive Dirac fermion on the surface of a magnetically doped topological insulator. *Science* **2010**, *329*, 659–662.

[47] Wu, L.; Salehi, M.; Koirala, N.; Moon, J.; Oh, S.; Armitage, N. Quantized Faraday and Kerr rotation and axion electrodynamics of a 3D topological insulator. *Science* **2016**, *354*, 1124–1127.

[48] Wu, L.; Tse, W.-K.; Brahlek, M.; Morris, C.; Aguilar, R. V.; Koirala, N.; Oh, S.; Armitage, N. High-resolution Faraday rotation and electron-phonon coupling in surface states of the bulk-insulating topological insulator Cu 0.02 Bi 2 Se 3. *Physical review letters* **2015**, *115*, 217602.

[49] Pan, L.; Liu, X.; He, Q. L.; Stern, A.; Yin, G.; Che, X.; Shao, Q.; Zhang, P.; Deng, P.; Yang, C.-Y., et al. Probing the low-temperature limit of the quantum anomalous Hall effect. *Science advances* **2020**, *6*, eaaz3595.

[50] Lachman, E. O.; Young, A. F.; Richardella, A.; Cuppens, J.; Naren, H.; Anahory, Y.; Meltzer, A. Y.; Kandala, A.; Kempinger, S.; Myasoedov, Y., et al. Visualization of superparamagnetic dynamics in magnetic topological insulators. *Science advances* **2015**, *1*, e1500740.

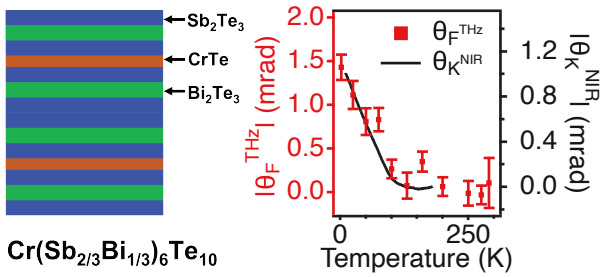
Sb2Te3
CrTe
Bi2Te3
Cr(Sb2/3Bi1/3)6Te10
2.0
1.5
1.0
0.5
0.0
|θF THz| (mrad)
θF THz
θK NIR
1.2
0.8
0.4
0.0
|θK NIR| (mrad)
0
250
Temperature (K)

TOC Graphic